Solution of Incompressible Turbulent Flow by a Mesh-Free Method

R. Vertnik[1] and B. Šarler[2]

Abstract: The application of the mesh-free Local Radial Basis Function Collocation Method (LRBFCM) in solution of incompressible turbulent flow is explored in this paper. The turbulent flow equations are described by the low - Re number k-ε model with Jones and Launder [Jones and Launder (1971)] closure coefficients. The involved velocity, pressure, turbulent kinetic energy and dissipation fields are represented on overlapping 5-noded sub-domains through collocation by using multiquadrics Radial Basis Functions (RBF). The involved first and second derivatives of the fields are calculated from the respective derivatives of the RBF's. The velocity, turbulent kinetic energy and dissipation equations are solved through explicit time stepping. The pressure-velocity coupling is calculated iteratively, based on the Chorin's fractional step method [Chorin, 1967]. The adaptive upwinding technique, proposed by the Lin and Atluri [Lin and Atluri (2000)] is used because of the convection dominated situation. The solution procedure is represented in 2D. Three test cases have been performed: laminar flow in a channel with $Re = 100$, turbulent flow in a channel with $Re = 12300$ and turbulent flow in a channel with 1/3 backward facing step with $Re = 5000$. The solution is compared with the analytical solution in the first case, with the experiment [Laufer (1948)] and commercial code Fluent in the second case, and with the experiment [Jović and Driver (1994)], commercial code Fluent and direct numerical simulation [Le, Moin and Kim (1997)] in the third case. All numerical examples include non-uniform spatial discretisation. A reasonably good agreement between the solutions has been achieved. The advantages of the represented mesh-free approach are its simplicity, accuracy, similar coding in 2D and 3D, and straightforward applicability in non-uniform node arrangements.

[1] Štore-Steel, Techical Development, E-mail: robert.vertnik@p-ng.si
[2] University of Nova Gorica, Laboratory for Multiphase Processes, Slovenia, E-mail: bozidar.sarler@p-ng.si

31 facing step

1   Introduction

33 In recent years, a number of mesh-free methods () [Atluri and Shen (2002), Atluri
34 (2004), Liu (2003), Liu and Gu (2005)] have been developed to circumvent the
35 problem of polygonisation encountered in the classical numerical methods (finite
36 difference (FDM) and finite volume (FVM) method, finite element method (FEM),
37 boundary domain integral method (BDIM)). In mesh-free methods, approximation
38 is constructed entirely in terms of a set of nodes. There exist a number of meshless
39 methods such as the Element free Galerkin methods, the Meshless local Petrov-
40 Galerkin method, the Point interpolation method, the Point assembly method, the
41 Finite point method, the Finite difference method with arbitrary irregular grids,
42 Smoothed particle hydrodynamics, Reproducing kernel particle method, etc. A
43 class of such methods is based on collocation with radial basis functions [Šarler
44 (2007)]. These functions [Buhmann (2000)] have been first under intensive re-
45 search in multivariate data and function interpolation [Franke (1982)]. Kansa used
46 them for scattered data approximation [Kansa (1990a)] and than for the solution of
47 partial differential equations [Kansa (1990b)]. The key point of the Radial Basis
48 Function Collocation Method (RBFCM) or Kansa Method (KM) for solving the
49 PDEs is the approximation of the fields on the boundary and in the domain by a
50 set of global approximation functions. The discretization is, respectively, repre-
51 sented only by grid-points (poles of the global approximation functions) in contrast
52 to FEM and BDIM methods where appropriate polygonisation needs to be gener-
53 ated in addition, or FDM, where points are constrained to the coordinate lines. The
54 main advantage of using the RBFCM for solution of partial differential equations
55 is its simplicity, applicability to different PDEs, and effectiveness in dealing with
56 arbitrary dimension and complicated domains. The method recently started to be
57 applied in many scientific and engineering disciplines. It has been first used in the
58 heat transport context by [Zerroukat, Power and Chen (1998)]. The method has
59 been afterwards applied to the classical De Vahl Davis natural convection problem
60 by asymmetric collocation in [Šarler, Perko, Chen and Kuhn (2001)] and addition-
61 ally by the symmetric and modified collocation in [Šarler (2005)]. The method was
62 used for solution of the Stefan problems [Kovačević, Poredoš and Šarler (2003)],
63 wave equations [Haq, ul-Islam and Ali (2008)] and solid mechanics problems [Mai-
64 Duy, Khennane and Tran-Cong (2007), Le, Mai-Duy, Tran-Cong and Baker (2008)]
65 as well. The method has been formulated instead of deriving the RBF's by integrat-
66 ing the partial derivatives [Mai-Duy, Tran-Cong. (2003)] and applied to transient
67 problems [Mai-Cao and Tran-Cong (2005)] fluid flow [Mai-Duy, Mai-Cao, Tran-
68 Cong, (2007)] and moving boundaries [Mai-Cao and Tran-Cong (2008)]. Several

69 other special developments of the method have been deduced such as the improved
70 treatment of the Neumann boundary conditions [Libre, Emdadi, Kansa, Rahimian
71 and Shekarchi (2008)].

72 The main disadvantage of the mentioned method represent the related full matrices
73 that are very sensitive to the choice of the free parameter in RBFs and are diffi-
74 cult to solve for problems of the order of 10^3 unknowns or larger. The solution of
75 related problem has been attempted by domain decomposition [Mai-Duy and Tran-
76 Cong (2002)], multi-grid approach and compactly supported RBFs [Chen, Ganesh,
77 Golberg and Cheng (2002)] which all represent a substantial complication of the
78 original simple method. The radial basis functions have been first put into context
79 of porous media flow by [Šarler, Gobin, Goyeau, Perko and Power (2000)] where
80 the natural convection problem in Darcy porous media, and later Darcy-Brinkman
81 porous media [Šarler, Perko, Gobin, Goyeau and Power (2004)] have been solved
82 by the dual reciprocity boundary element method (DRBEM). This method belongs
83 to the semi-mesh-free methods, because the domain fields are approximated by the
84 global interpolation with the RBFs and the boundary fields by the boundary ele-
85 ments (polygons). The truly mesh-free RBFCM has been for the first time used
86 for solution of Darcy porous media in [Šarler, Perko and Chen (2004)]. A sub-
87 stantial breakthrough in the development of the RBFCM was its local formulation,
88 LRBFCM. This formulation was first developed for diffusion problems [Šarler and
89 Vertnik (2006)], than to convection-diffusion problems with phase-change [Vertnik
90 and Šarler (2006)], to industrial application of direct chill casting of aluminum al-
91 loys [Vertnik, Zalonik and Šarler (2006)], continuous casting of steel [Vertnik and
92 Šarler (2008)], to solid-solid phase transformations [Kovačević and Šarler (2005)]
93 and to solution of Navier Stokes equations [Divo and Kassab (2007), Kosec and
94 Šarler (2008a)] and porous media flow [Kosec and Šarler (2008b)]. A similar, local
95 quadrature based RBF approach, was developed by [Shu, Ding and Yeo (2005)].
96 The main issue of the local version of the RBFCM is the collocation on a sub-set
97 of, in general, overlapping sub-domains, which drastically reduces the collocation
98 matrix size on the expense of solving many small matrices instead of a large one.
99 Since the method does not experience significant accuracy drawback in compari-
100 son with the global version, it represents a practical choice also for solving very
101 large problems. The main goal of this work is to upgrade the LRBFCM for solv-
102 ing complex engineering turbulence models, which is by the best knowledge of the
103 present authors, a pioneering effort in the development of the meshless methods.
104 In the last century, a lot of research has been devoted towards understanding of
105 the turbulent flows. In spite of those attempts, a general physical theory still does
106 not exist. Numerically, those flows could be very well predicted by the direct nu-
107 merical simulation (DNS) of the Navier-Stokes equations. Unfortunately, in the

108 DNS very fine spatial discretization has to be used in order to model and track all
109 eddies of the flow, especially the smallest ones. The applicability of the DNS is
110 currently limited to very simple geometries and for turbulent flows with moderate
111 Reynolds (Re) numbers [Le, Moin and Kim (1997)]. Other turbulent models are
112 mainly derived through the time-averaging of the Navier-Stokes (N-S) equations.
113 Due to the nonlinearity of the time-averaged N-S equations, a closure problem
114 arises (more unknowns than equations), which puts these family of models into the
115 category of semi-empirical ones. Various models were proposed [Wilcox (1993)],
116 which are rather old, but still in use nowadays. Probably the most known and rep-
117 resentative is the family of two-equation k-ε models, which are further divided into
118 two groups, standard and low-Re models. The standard k-ε models use the wall-
119 functions, while the low-Re models use special closure coefficients to correctly
120 predict the turbulent boundary layers. Better predictions are obtained with the low-
121 Re models, but a very fine disretization near the walls is required. In this work,
122 the low-Re k-ε model is used with the closure coefficients proposed by [Jones and
123 Launder (1971)].

124 The present paper is structured in the following way. The governing equations
125 of the incompressible turbulent flow are presented first. The general initial and
126 boundary conditions for the velocity, pressure, turbulent kinetc energy k and dissi-
127 pation ε are described. The explicit solution procedure of the governing equations
128 is proposed, where the fractional step method [Chorin (1967)] is used to couple
129 the velocity and pressure fields. The discretization is made by the LRBFCM by
130 using multiquadrics on five-noded sub-domains. Due to the convection-dominated
131 problems, the adaptive upwind technique (AUT) is introduced. At the end, the pro-
132 posed numerical method is assessed through three numerical examples: laminar
133 two-dimensional channel flow, turbulent two-dimensional channel flow, and turbu-
134 lent flow over a backward-facing step. The results are compared with the analytical
135 solution, experiments, DNS and the most recent version 6.3 of the commercial soft-
136 ware Fluent.

137 2 Governing equations

Consider a connected fixed domain Ω with boundary Γ filled with a fluid that ex-
hibits incompressible turbulent flow. The flow is described (in a two-dimensional
Cartesian coordinate system with base vectors $\mathbf{i}_\varsigma$; $\varsigma = x, y$ and coordinates p_ς; $\varsigma =
x, y$, i.e. position of point $\mathbf{p}$ is determined as $\mathbf{p} = \mathbf{i}_\varsigma p_\varsigma$; $\varsigma = x, y$) by the following
time-averaged Reynolds equations for mass conservation, and momentum conser-
vation in x and y directions

$$\frac{\partial v_x}{\partial p_x} + \frac{\partial v_y}{\partial p_y} = 0, \tag{1}$$

$$\frac{\partial v_x}{\partial t} + v_x \frac{\partial v_x}{\partial p_x} + v_y \frac{\partial v_x}{\partial p_y} =$$
$$- \frac{1}{\rho} \frac{\partial p}{\partial p_x} + \frac{\partial}{\partial p_x} \left(v + v_t \right) \left(2 \frac{\partial v_x}{\partial p_x} \right) + \frac{\partial}{\partial p_y} \left(v + v_t \right) \left(\frac{\partial v_x}{\partial p_y} + \frac{\partial v_y}{\partial p_x} \right), \quad (2)$$

$$\frac{\partial v_y}{\partial t} + v_x \frac{\partial v_y}{\partial p_x} + v_y \frac{\partial v_y}{\partial p_y} =$$
$$- \frac{1}{\rho} \frac{\partial p}{\partial p_y} + \frac{\partial}{\partial p_y} \left(v + v_t \right) \left(2 \frac{\partial v_y}{\partial p_y} \right) + \frac{\partial}{\partial y} \left(v + v_t \right) \left(\frac{\partial v_y}{\partial p_x} + \frac{\partial v_x}{\partial p_y} \right), \quad (3)$$

with v_x and v_y standing for the time averaged velocity components in x- and y-direction, respectively, and p, t, ρ, v and v_t standing for pressure, time, density, molecular kinematic viscosity and turbulent kinematic viscosity, respectively. Molecular kinematic viscosity is defined as

$$v = \frac{\mu}{\rho} \quad (4)$$

where μ is molecular dynamic viscosity. Turbulent kinematic viscosity is defined as

$$v_t = c_\mu f_\mu \frac{k^2}{\varepsilon}. \quad (5)$$

In Eq. (5) c_μ and f_μ are closure coefficients of the turbulence model, and k and ε are the turbulent kinetic energy and dissipation, calculated by the following transport equations

$$\frac{\partial k}{\partial t} + v_x \frac{\partial k}{\partial p_x} + v_y \frac{\partial k}{\partial p_y} =$$
$$\frac{\partial}{\partial p_x} \left(v + \frac{v_t}{\sigma_k} \right) \frac{\partial k}{\partial p_x} + \frac{\partial}{\partial p_y} \left(v + \frac{v_t}{\sigma_k} \right) \frac{\partial k}{\partial p_y} + P_k - \varepsilon + D, \quad (6)$$

$$\frac{\partial \varepsilon}{\partial t} + v_x \frac{\partial \varepsilon}{\partial p_x} + v_y \frac{\partial \varepsilon}{\partial p_y} =$$
$$\frac{\partial}{\partial p_x} \left(v + \frac{v_t}{\sigma_\varepsilon} \right) \frac{\partial \varepsilon}{\partial p_x} + \frac{\partial}{\partial p_y} \left(v + \frac{v_t}{\sigma_\varepsilon} \right) \frac{\partial \varepsilon}{\partial p_y} + (c_{1\varepsilon} f_1 - c_{2\varepsilon} f_2 \varepsilon) \frac{\varepsilon}{k} + E, \quad (7)$$

where P_k, D and E are the shear production of turbulent kinetic energy, source term in k equation and source term in ε equation, respectively. They are given by

$$P_k = v_t \left(2 \left(\frac{\partial v_x}{\partial p_x} \right)^2 + 2 \left(\frac{\partial v_y}{\partial p_y} \right)^2 + \left(\frac{\partial v_x}{\partial p_y} + \frac{\partial v_y}{\partial p_x} \right)^2 \right), \quad (8)$$

$$D = -2\nu \left[\left(\frac{\partial \sqrt{k}}{\partial p_x} \right)^2 + \left(\frac{\partial \sqrt{k}}{\partial p_y} \right)^2 \right], \tag{9}$$

$$E = 2\nu\nu_t \left[\left(\frac{\partial^2 v_x}{\partial p_y^2} \right)^2 + \left(\frac{\partial^2 v_y}{\partial p_x^2} \right)^2 \right], \tag{10}$$

In Eqs. (5) and (7), the closure coefficients c_μ, f_μ, $c_{1\varepsilon}$, f_1, $c_{2\varepsilon}$, f_2, σ_k and σ_ε of the low-Reynolds turbulent model [Jones and Launder (1971)] are defined as

$$c_\mu = 0.09, \tag{11}$$

$$f_\mu = \exp \left(\frac{-2.5}{1 + Re_t/50} \right), \tag{12}$$

$$c_{1\varepsilon} = 1.45, \tag{13}$$

$$f_1 = 1.0, \tag{14}$$

$$c_{2\varepsilon} = 2.00, \tag{15}$$

$$f_2 = 1 - 0.3 \exp \left(-Re_t^2 \right), \tag{16}$$

$$\sigma_k = 1.0, \tag{17}$$

$$\sigma_\varepsilon = 1.3. \tag{18}$$

The turbulent Reynolds number Re_t (used in Eqs. (12) and (16)) is defined as

$$Re_t = \frac{k^2}{\nu\varepsilon} \tag{19}$$

138 In order to determine the turbulent flow, the system of Eqs. (1), (2), (3), (6) and (7)
139 has to be solved.

140 ## 3 Solution procedure

141 We seek the solution of the x and y velocity components, pressure field, k and ε
142 fields at time $t + t_0$ by assuming known fields v_x, v_y, p, k and ε at time t_0 and known
143 boundary conditions. The coupled set of mass conservation Eq. (1) and momentum
144 conservation Eqs. (2),(3) are solved by the fractional step method [Chorin (1967)],
145 where the continuity of the mass Eq. (1) is considered by constructing and solving
146 the pressure Poisson equation. At every time step, the following explicit numerical
147 algorithm is used

Step 1: The intermediate velocity components v_x^* and v_y^* are calculated first, without
considering the pressure gradient

$$
\begin{aligned}
v_x^* = v_{x0}^+ \frac{\rho}{\Delta t} \\
\left[-v_x \frac{\partial v_x}{\partial p_x} - v_y \frac{\partial v_x}{\partial p_y} + \frac{\partial}{\partial p_x} (\nu + \nu_t) \left(2 \frac{\partial v_x}{\partial p_x} \right) + \frac{\partial}{\partial y} (\nu + \nu_t) \left(\frac{\partial v_x}{\partial p_y} + \frac{\partial v_y}{\partial p_x} \right) \right]_0,
\end{aligned}
\tag{20}
$$

$$
\begin{aligned}
v_y^* = v_{y0}^+ \frac{\rho}{\Delta t} \\
\left[-v_x \frac{\partial v_y}{\partial p_x} - v_y \frac{\partial v_y}{\partial p_y} + \frac{\partial}{\partial p_y} (\nu + \nu_t) \left(2 \frac{\partial v_y}{\partial p_y} \right) + \frac{\partial}{\partial y} (\nu + \nu_t) \left(\frac{\partial v_y}{\partial p_x} + \frac{\partial v_x}{\partial p_y} \right) \right]_0,
\end{aligned}
\tag{21}
$$

where index 0 represents initial conditions at time $t = t_0$. Step 2: The pressure
Poisson equation is solved

$$
\nabla^2 p = \frac{\rho}{\Delta t} \left(\frac{\partial v_x^*}{\partial p_x} + \frac{\partial v_y^*}{\partial p_y} \right)
\tag{22}
$$

148 The pressure equation can be solved by converting it into a diffusion equation [Divo
149 and Kassab (2007)] or by solving the sparse matrix [Lee, Liu and Fan (2003)]. An
150 additional possibility represents the use of the local pressure correction [Kosec and
151 Šarler (2008)] which seems to be most efficient. However the last correction has
152 not been yet successfully tested for inflow and outflow situations. In this work,
153 the approach by Lee, Liu and Fan (2003) is used, where the solution of the sparse
154 matrix is solved by the direct method. In case of the fixed node arrangement, the
155 left-hand side of the sparse matrix can be L-U decomposed before the first time
156 step. This numerical approach significantly improves the performance, since only
157 the back substitution is used to solve the pressure field at each time step. The
158 boundary conditions for the pressure equation are explicitly given in the Section 5.

Step 3: The intermediate velocity components are corrected through the calculated pressure gradient at time $t = t_0 + \Delta t$

$$v_x = v_x^* - \frac{\Delta t}{r} \frac{\partial p}{\partial p_x}, \tag{23}$$

$$v_y = v_y^* - \frac{\Delta t}{r} \frac{\partial p}{\partial p_y}, \tag{24}$$

Step 4: After the solution of the velocity field, given in steps $1 \div 3$, the transport Eqs. (6) and (7) of the turbulence model at time $t = t_0 + \Delta t$ are solved

$$k = k_0 + \Delta t \left[-v_x \frac{\partial k}{\partial p_x} - v_y \frac{\partial k}{\partial p_y} + \frac{\partial}{\partial p_x} \left(v + \frac{v_t}{\sigma_k} \right) \frac{\partial k}{\partial p_x} + \frac{\partial}{\partial p_y} \left(v + \frac{v_t}{\sigma_k} \right) \frac{\partial k}{\partial p_y} + P_k - \varepsilon + D \right]_0, \tag{25}$$

$$\varepsilon = \varepsilon_0 + \Delta t \left[-v_x \frac{\partial \varepsilon}{\partial p_x} - v_y \frac{\partial \varepsilon}{\partial p_y} + \frac{\partial}{\partial p_x} \left(v + \frac{v_t}{\sigma_\varepsilon} \right) \frac{\partial \varepsilon}{\partial p_x} + \frac{\partial}{\partial p_y} \left(v + \frac{v_t}{\sigma_\varepsilon} \right) \frac{\partial \varepsilon}{\partial p_y} + (c_{1\varepsilon} f_1 - c_{2\varepsilon} f_2 \varepsilon) \frac{\varepsilon}{k} + E \right]_{t=t_0}. \tag{26}$$

Step 5: The turbulent viscosity is updated from Eq. (5), and the solution is ready for the next time step.

The block diagram of the described algorithm is schematically represented in Figure 3.1.

4   Initial conditions

It is well known that all involved four transport Eqs. (20), (21),(25) and (26) are strongly coupled. So it is very important how we choose the initial conditions for each transport variable. The initial conditions for velocity components are obtained by solving the potential field

$$\nabla^2 \phi = 0 \tag{27}$$

where ϕ stands for the velocity potential. Laplace equation (27) is solved by the same approach as pressure equation (22). The following boundary conditions are used
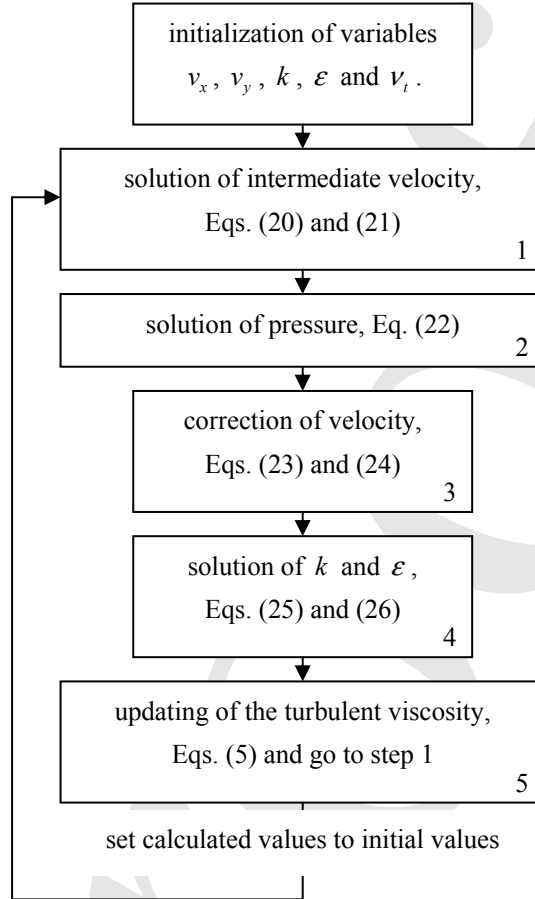
Figure 3.1: Block diagram of the numerical algorithm.

At the inlet boundaries and solid walls, the Neumann boundary conditions for velocity potential are prescribed

$$\frac{\partial \phi}{\partial p_x} n_x + \frac{\partial \phi}{\partial p_y} n_y = -(v_{0x} n_x + v_{0y} n_y) \tag{28}$$

At the outlet boundaries, the Dirichlet boundary conditions for velocity potential are set to

$$\phi = 0 \tag{29}$$

After solving the potential flow field, the velocity field in the domain is obtained

by the following relations

$$v_{0x} = \frac{\partial \phi}{\partial p_x}, \quad v_{0y} = \frac{\partial \phi}{\partial p_y} \tag{30}$$

167 This procedure guarantees the solenoidality of the initial velocity field.

168 In order to prescribe the proper initial conditions for k and ε, two different tech-
169 niques might be employed:

170 Use of the uniform profile for both k and ε. A few thousand time steps must usually
171 be performed with smaller time step to achieve the consistency between the veloc-
172 ity, pressure, turbulent energy and dissipation equation. When the large mismatch
173 of the transport variables at initial times is reduced, larger time steps can be used.

174 Use of the assumption of turbulent equilibrium [Yoder and Georgiadis (1999)],
175 where the production of turbulent kinetic energy equals the rate of dissipation. In
176 order to use this technique, another turbulence model, usually algebraic model, is
177 first run to get initial values of the turbulent viscosity.

178 In this work, the turbulence transport variables are initialized by the first approach.

179 5   Boundary conditions

180 Four different types of boundaries are considered in the present paper: inlet, outlet,
181 symmetry, and wall. The following boundary conditions are used at these bound-
182 aries:

183   • At the inlet boundary, the Dirichlet boundary conditions for velocity compo-
184   nents, k and ε are prescribed.

185   • At the outlet boundary, the Neumann boundary conditions for velocity com-
186   ponents, k and ε are prescribed and set to zero.

187   • At the symmetry line, the same Neumann boundary conditions as for the
188   outlet boundary are used, except for the velocity component, perpendicular
189   to the symmetry line, where the Dirichlet boundary conditions are prescribed
190   and set to zero.

191   • At the wall, the Dirichlet no-slip boundary conditions are set, which implies
192   that the velocity components, k and ε are all set to zero.

Boundary conditions for pressure Eq. (22) at inlet, symmetry, and wall boundaries
are of the Neumann type, i.e.,

$$\frac{\partial p}{\partial p_x} n_x + \frac{\partial p}{\partial p_y} n_y = \frac{1}{\Delta t} \left(\varphi_x n_x + \varphi_y n_y \right) \tag{31}$$

where the n_x and n_y are the components of the normal vector in x and y directions. φ_x and φ_y have the following form

$$\varphi_x = v_x^* - v_{x,0}^w \tag{32}$$

$$\varphi_y = v_y^* - v_{y,0}^w \tag{33}$$

where v_x^* and v_y^* are intermediate velocities, solved by the Eqs. (20) and (21) at the wall. In Eqs. (32) and (33), the $v_{x,0}^w$ and $v_{y,0}^w$ represents the wall velocities at t_0. At the outlet boundary, the Dirichlet boundary conditions for pressure are used and set to zero.

6 Radial basis function collocation method

The representation of function Φ over a set of l (in general) non-equally spaced $_lN$ nodes $_l\mathbf{p}_n$; $n = 1, 2, \ldots, _lN$ is made in the following way

$$\Phi(\mathbf{p}) \approx \sum_{k=1}^{_lK} {}_l\psi_k(\mathbf{p}) {}_l\alpha_k \tag{34}$$

$_l\psi_k$ stands for the shape functions, $_l\alpha_k$ for the coefficients of the shape functions, and $_lK$ represents the number of the shape functions. The left lower index on entries of Eq. (34) represents the domain of influence $_l\omega$ on which the coefficients $_l\alpha_k$ are determined. The domains of influence $_l\omega$ can in general be contiguous (overlapping) or non-contiguous (non-overlapping). Each of the domains of influence $_l\omega$ includes $_lN$ grid-points of which $_lN_\Omega$ are in the domain and $_lN_\Gamma$ are on the boundary. Typical domains of influence are shown in Figure 6.1.

The coefficients can be calculated from the nodal values in the domain of influence in two distinct ways. The first way is collocation (interpolation) and the second way is approximation by the least squares method. Only the more simple collocation version for calculation of the coefficients is considered in this paper. Let us assume the known function values $_l\Phi_n$ in the nodes $_l\mathbf{p}_n$ of the domains of influence $_l\omega$. The collocation implies

$$\Phi(_l\mathbf{p}_n) = \sum_{k=1}^{_lN} {}_l\psi_k(_l\mathbf{p}_n) {}_l\alpha_k \tag{35}$$

For the coefficients to be computable, the number of the shape functions has to match the number of the collocation points $_lK = _lN$, and the collocation matrix has to be non-singular. The system of Eqs. (35) can be written in a matrix-vector notation

$$_l\psi {}_l\boldsymbol{\alpha} = {}_l\boldsymbol{\Phi}; \quad _l\psi_{kn} = {}_l\psi_k(_l\mathbf{p}_n); \quad _l\Phi_n = \Phi(_l\mathbf{p}_n) \tag{36}$$
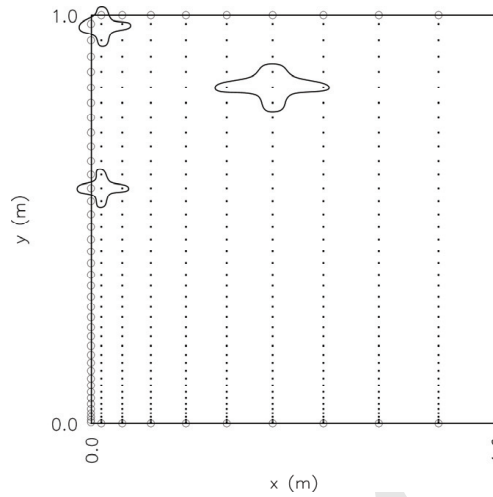
Figure 6.1: Typical corner, boundary, and interior 5-noded domains of influence.

The coefficients $_l\boldsymbol{\alpha}$ can be computed by inverting the system (14)

$$_l\boldsymbol{\alpha} =\, _l\boldsymbol{\psi}^{-1}\,_l\boldsymbol{\Phi} \tag{37}$$

By taking into account the expressions for the calculation of the coefficients $_l\alpha$, the collocation representation of function $\Phi(\mathbf{p})$ on domain of influence $_lw$ can be expressed as

$$\Phi(\mathbf{p}) \approx \sum_{k=1}^{lN}\,_l\psi_k(\mathbf{p}) \sum_{n=1}^{lN}\,_l\psi_{kn}^{-1}\,_l\Phi_n \tag{38}$$

The first partial spatial derivatives of $\Phi(\mathbf{p})$ in the domain of influence $_lw$ can be expressed as

$$\frac{\partial}{\partial p_\varsigma}\Phi(\mathbf{p}) \approx \sum_{k=1}^{lN}\frac{\partial}{\partial p_\varsigma}\,_l\psi_k(\mathbf{p}) \sum_{n=1}^{lN}\,_l\psi_{kn}^{-1}\,_l\Phi_n; \quad \varsigma = x, y \tag{39}$$

The second partial spatial derivatives of $\Phi(\mathbf{p})$ in the domain of influence $_lw$ can be expressed as

$$\frac{\partial^2}{\partial p_\varsigma p_\xi}\Phi(\mathbf{p}) \approx \sum_{k=1}^{lN}\frac{\partial^2}{\partial p_\varsigma p_\xi}\,_l\psi_k(\mathbf{p}) \sum_{n=1}^{lN}\,_l\psi_{kn}^{-1}\,_l\Phi_n;$$

$$\varsigma, \xi = x, y \tag{40}$$

The radial basis functions, such as multiquadrics, can be used for the shape function

$$_l\psi_k(\mathbf{p}) = \left[_l r_k^2 + c^2\right]^{1/2} \tag{41}$$

where c represents the shape parameter and $_l r_0$ the radial distance between two points in the sub-domain. The $_l r_k$ is scaled by the maximum distance between sub-domain points in x and y direction

$$_l r_k^2 = \left(\frac{p_x - p_{kx}}{p_{x\,\max}}\right)^2 + \left(\frac{p_y - p_{ky}}{p_{y\,\max}}\right)^2 \tag{42}$$

205 where $p_{x\,\max}$ is the maximum distance between any of the sub-domain points in
206 the x direction and $p_{y\,\max}$ is the maximum distance between any of the sub-domain
207 points in the y direction.

208 The shape parameter c is fixed for all sub-domains, and set to 32 [Šarler and Vertnik
209 (2006), Vertnik and Šarler (2006)] in all numerical examples of the present paper.
210 The accuracy of the results increases with increased value of the shape parame-
211 ter, however the condition number of the collocation matrix worsens. The chosen
212 value 32 represents a reasonable balance between both trends. All sub-domains are
213 chosen to contain five nodes as depicted in Figure 6.1.

214 7 Adaptive upwind technique

215 The turbulent flows belong to the convection dominated problems. If the spatial
216 discretization is not sufficiently fine, the solution becomes instable or oscillatory.
217 Without any additional numerical efforts, the LRBFCM on uniform node spac-
218 ing, gives similar oscillations as the central FDM discretization on uniform node
219 spacing, i.e. the solution starts to oscillate when the Péclet number (based on the
220 node spacing) is greater than two. To stabilize the numerical solution, the adap-
221 tive upwind technique [Lin and Atluri (2000)] is used, where the adaptive upwind
222 displacement is constructed based on the local Péclet number. This technique was
223 already found to be very useful in the numerical modeling of the heat transfer in
224 the continuous casting of steel [Vertnik, Šarler, Bulinski and Manojlović (2007)].

In the adaptive upwind support technique, the expansion coefficients are first calcu-
lated by the LRBFCM. The derivatives of the convection terms are then calculated
in the point $p_{\varsigma\Delta}$, shifted by the central offset distance Δp_ς in the opposite direc-
tion of the current velocity, see Figure 7.1. The position of the shifted point $p_{\Delta\varsigma}$ is
defined as

$$p_{\Delta\varsigma} = p_\varsigma - \Delta p_\varsigma; \quad \varsigma = x, y \tag{43}$$

The central offset distance is calculated by

$$\Delta p_\varsigma = \text{sign}(v_x)\,\delta\frac{h}{2}; \quad \varsigma = x,y \tag{44}$$

where δ is the upwind function and h is the maximal distance between the central point and the neighboring point in the opposite direction of the velocity, as shown in Figure 7.1. The upwind function, represented in Figure 7.2, is defined as

$$\delta = \coth\left|Pe_\varsigma\right| - \frac{1}{\left|Pe_\varsigma\right|}; \quad \varsigma = x,y \tag{45}$$

and the local Péclet number as

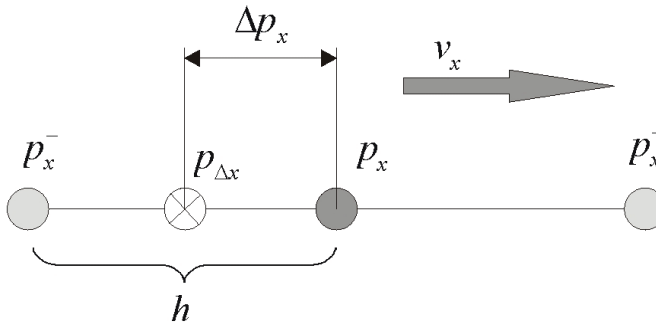$$Pe = \frac{v_x\left(p_x^+ - p_x^-\right)}{\nu + \nu_t} \tag{46}$$

Figure 7.1: Adaptive upwind support in x-direction.

225

8 Numerical examples

226

227 Three numerical examples are represented in the present work. The first example
228 shows the ability of the developed numerical method to solve the laminar incom-
229 pressible flows. The second example employs the same geometry as the first ex-
230 ample, but with included turbulence. The last example represents a well known
231 test for various turbulence models: a 1/3 backward-facing step channel flow. In all
232 three examples, the time step Δt is equal to 10^{-3} s and kept constant through the
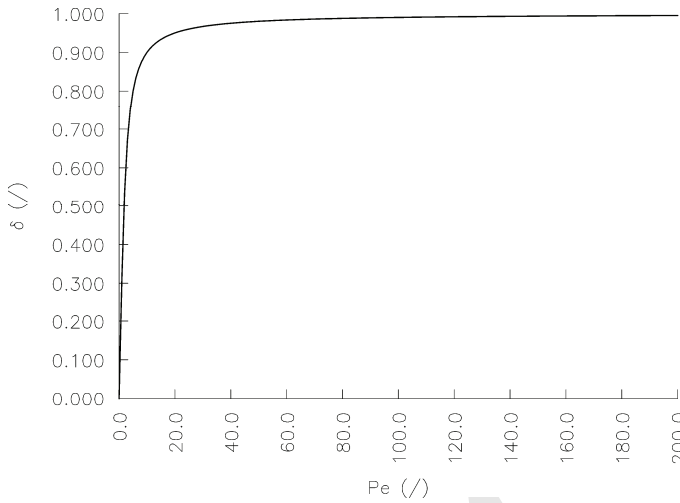233 entire simulation.

Figure 7.2: Upwind function.

234 **8.1 Laminar 2D channel flow**

The physical domain is a 2D channel with length L and height D. In our computations, only one half of a channel with height $H = D/2$ is considered, as shown in Figure 8.1. The length of the channel is large enough to achieve the fully developed flow at the channel outlet. The density and the inlet velocity are both equal to unity, while the kinematic viscosity ν is calculated from the Reynolds number
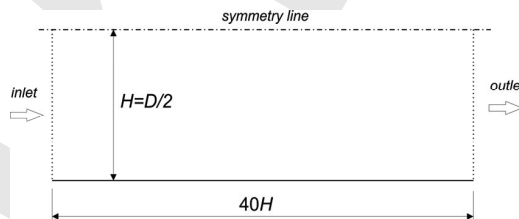
$$Re = \frac{v_x \cdot H}{\nu}. \tag{47}$$

Figure 8.1: Geometry of the 2D channel flow.

The computation was performed with $Re_H = 100$, where $H = 1.0\,m$. The irregular node arrangement with 4137 nodes (41x101 nodes without 4 corner nodes) was
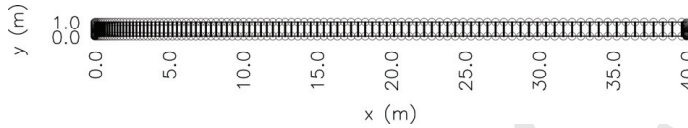
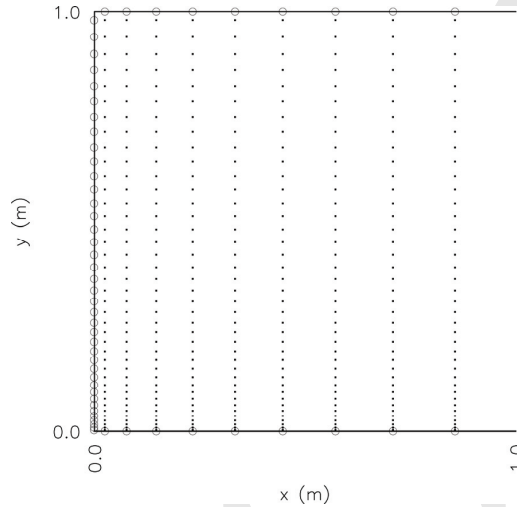Figure 8.2: The node arrangement with 4137 nodes.

Figure 8.3: The detailed view of the node arrangement. Points - interior nodes, circles - boundary nodes.

used. The arrangement is shown in Figure 8.2 and Figure 8.3. The calculated velocity v_x at the channel outlet was compared with the following analytical solution

$$v_{x,ana}(y) = \frac{3}{2}v_{x,inlet}\left(1 - \left(\frac{2y}{D}\right)^2\right) \tag{48}$$

235 The comparison is shown in Figure 8.4. An excellent agreement is observed be-
236 tween both solutions.

237 *8.2 Turbulent 2D channel flow*

The same geometry and node arrangement as used in the previous example is used in this example as well. Additionally, the turbulence model is included. The computation was performed with Reynolds number $Re_H = 12300$. The turbulent quan-
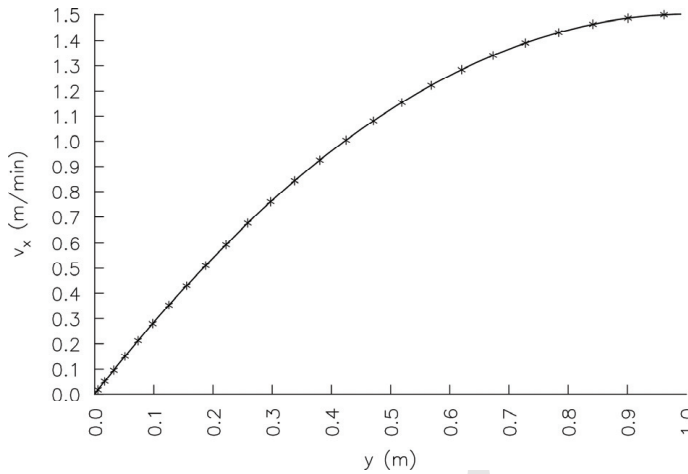
Figure 8.4: Horizontal velocity v_x at the channel outlet. Solid line - present method, symbols * – analytical solution.

tities at the inlet are defined by the following relations

$$k_{in} = \frac{3}{2}\left(i_0 \cdot v_{x,in}\right)^2, \quad \varepsilon_0 = C_\mu^{3/4}\frac{k_{in}^{3/2}}{0.07H} \tag{49}$$

238 where i is the turbulent intensity, set to 4 %. The results are compared with the
239 experiments [Laufer (1948)] and with the results obtained by the commercial soft-
240 ware Fluent. In Fluent, the calculation was performed by the uniform mesh with
241 64000 quadrilateral cells, and the k-ε turbulent model with standard wall functions
242 was set. The results are shown in Figure 8.5, where the normalized velocity v_x at the
243 channel outlet is shown. Numerical values of both numerical methods, evaluated at
244 the experiment positions, are tabulated in Table 1.

245 ## 8.3 *Backward facing step*

The geometry of the physical domain is taken from the experiment by [Jović and
Driver (1994)] and shown in Figure 8.6. The experiment is characterized by the
step height $H = 1.0$, the channel length after the step $L = 30H$ and by the Reynolds
number $Re_H = 5000$, which determines the inlet conditions at the step. The com-
putational domain considers only the physical domain after the step. In the experi-
ment, the fully developed flow was achieved at the $3H$ distance before the step with
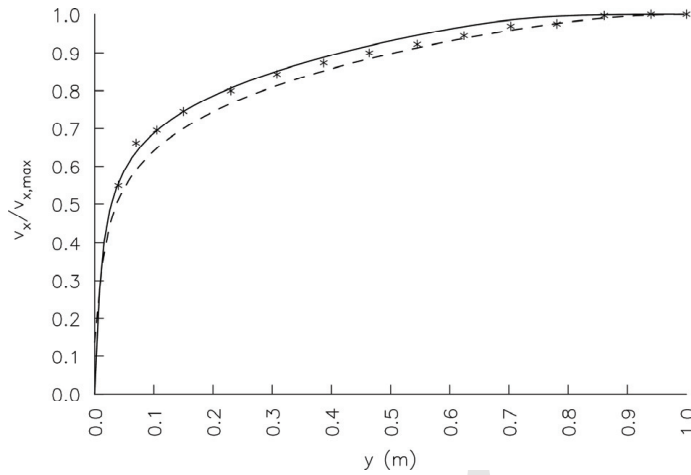the Reynolds number based on the momentum thickness $Re_\theta = 610$. The Re_θ is

Figure 8.5: Normalized velocity v_x at the channel outlet. Solid line – present method, dashed line – Fluent, and symbols * – measurements.

Table 1: Tabulated normalized velocity v_x at the channel outlet

y(m)	experiment[*]	present method	Fluent[♣]
0.040	0.5498	0.5541	0.5107
0.070	0.6615	0.6367	0.5897
0.105	0.6956	0.6943	0.6477
0.150	0.7449	0.7448	0.7002
0.230	0.7998	0.8067	0.7660
0.308	0.8434	0.8515	0.8134
0.387	0.8737	0.8884	0.8524
0.464	0.9000	0.9190	0.8845
0.545	0.9229	0.9468	0.9136
0.624	0.9456	0.9691	0.9383
0.703	0.9703	0.9858	0.9596
0.781	0.9759	0.9951	0.9770
0.861	0.9968	0.9988	0.9905
0.949	1.0000	0.9998	0.9982
1.000	1.0000	1.0000	1.0000

* [Laufer (1948)]

♣ Fluent, version 6.3

defined as

$$Re_\theta = \frac{\theta \cdot v_{x\Gamma}}{\nu} \tag{50}$$

246 where θ is the momentum thickness and $v_{x\Gamma}$ is the inlet velocity of the air, measured
247 in the channel far away upstream of the step. Both quantities are taken directly from
248 the experiment and have values $\theta = 0.12$ *cm* and $v_{x\Gamma} = 7.72 m/s$.

249 In order to achieve the same inlet conditions at the step as in the experiment, the
250 fully developed flow was first calculated with the 2D channel numerical simulation,
251 as described in the second example of this paper. The calculated profiles of v_x, v_y,
252 k, ε and v_t were considered as the inlet conditions of the channel at the step. Other
253 boundary conditions are the same as in the second example. The node arrangement
254 was generated with adaptation near the walls, see Figure 8.7. The detailed view of
255 the node arrangement near the walls is shown in Figure 8.8.

256 The results are compared with the measurements [Jović and Driver (1994)] (JD),
257 with the results obtained by the direct numerical simulation (DNS) of turbulent
258 flow [Le, Moin and Kim (1997)], and with the results obtained by the commercial
259 software (FLUENT).

260 In Fluent, the calculation was performed by the uniform mesh with 288000 cells
261 (mesh 1200×240 cells) and with the same turbulent model as in the first example.
262 With this very fine mesh, a reasonable mesh-independence of the results has been
263 achieved. The same boundary conditions and material properties were set as in the
LRBFCM calculations.
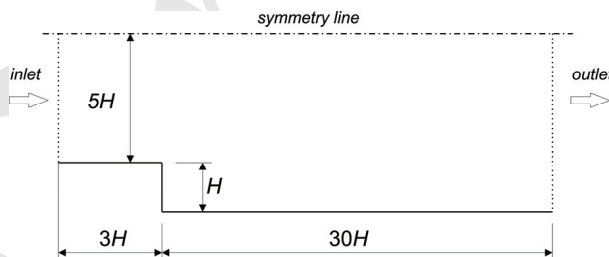
Figure 8.6: The physical domain of the backward-facing step.

264

265 The calculated velocity v_x at different x/H positions is compared with the results
266 obtained by other methods. For better insight of the obtained results, the velocity
267 v_x profile at each x/H position is plotted into its own figure: at $x/H = 4$ in Figure
268 8.10, at $x/H = 6$ in Figure 8.11, at $x/H = 10$ in Figure 8.12, at $x/H = 15$ in Figure
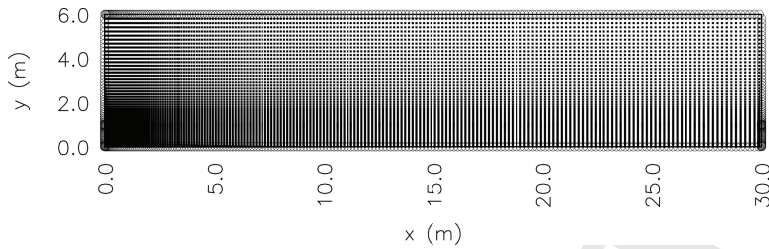
Figure 8.7: Node arrangement with 14267 nodes for geometry in Figure 8.6 (rotated for 90 deg.).
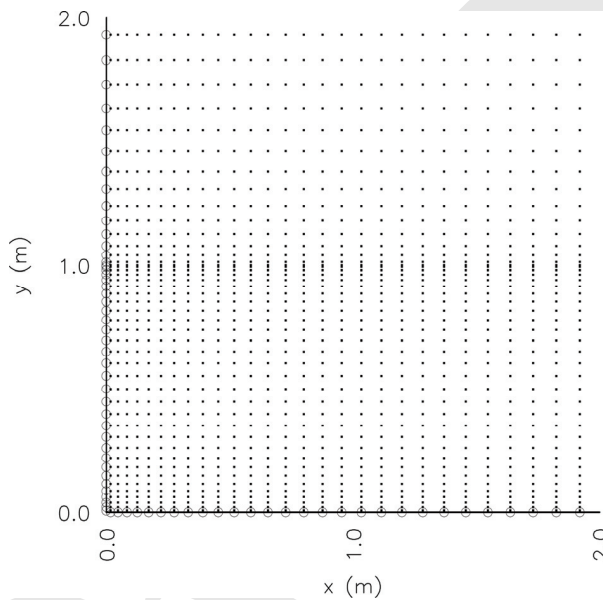
Figure 8.8: The detailed view of the node arrangement. Points - interior nodes, circles - boundary nodes.

8.13 and at $x/H = 19$ in Figure 8.14. Below each figure, the numerical and experimental velocity values v_x are also tabulated in Table 2, 3, 4, 5 and 6. The small differences between all methods and experiment are more clearly visible from the tabulated values. There are several reasons, why those differences are expected. The prevailing one is in using different turbulence models, where each model has its own advantages and weaknesses. DNS should probably be the most accurate, since the Navier-Stokes equations are directly solved.

The important quantity in the backward-facing step simulations is the reattachment
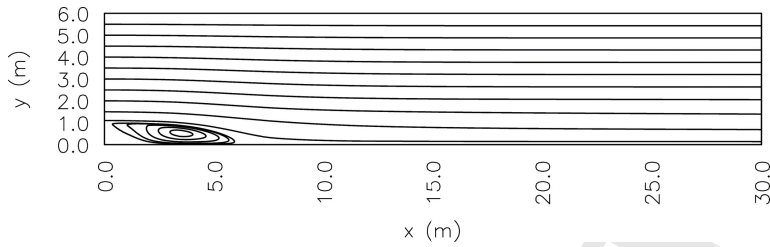
Figure 8.9: Streamlines calculated with the LRBFCM (rotated for 90 deg.).
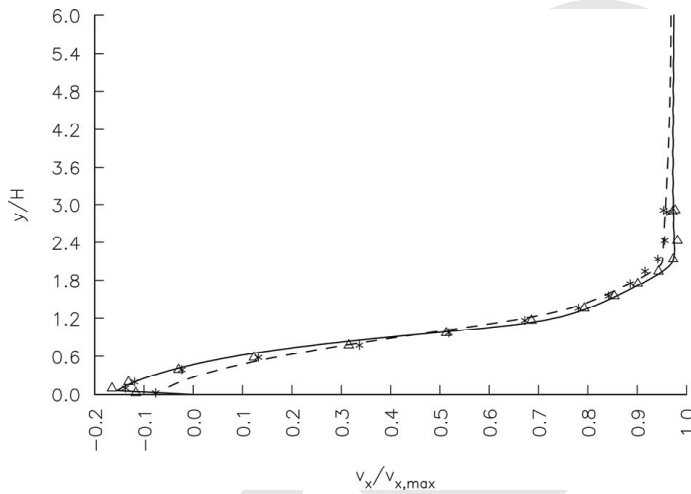
Figure 8.10: The normalized velocity v_x at $x/H = 4$. Solid line – LRBFCM, dashed line – FLUENT, Δ – DNS and * – JD.

277 length, were the fluid separates. The reattachment position can be obtained based
278 on the horizontal velocity v_x at the first inner point, closest to the bottom wall. The
279 separation is at the position were the velocity v_x is equal to zero. The separation po-
280 sition at $x/H = 6.28$ is obtained with the present method. The related reattachment
281 positions obtained by experiment and other numerical methods are represented in
282 Table 7.

283 *8.4 Global continuity calculation*

The global continuity of the RBF collocation method was checked for internal flows
in [Kosec and Šarler (2008a)]. In this paper, the global continuity is checked for
discussed three types of channel flows by calculating the mean velocity across the

Table 2: Normalized velocity v_x at $x/H = 4$.

	experiment[*]	present method	DNS[Δ]	FLUENT[♣]
0.025	-0.0764	-0.0634	-0.1164	-0.0621
0.097	-0.1373	-0.1463	-0.1647	-0.0546
0.194	-0.1192	-0.1193	-0.1314	-0.0272
0.388	-0.0233	-0.0419	-0.0299	0.0532
0.582	0.1321	0.0731	0.1230	0.1655
0.776	0.3368	0.2448	0.3153	0.3083
0.970	0.5181	0.4894	0.5129	0.4759
1.164	0.6723	0.7108	0.6857	0.6450
1.358	0.7811	0.8000	0.7928	0.7644
1.552	0.8420	0.8584	0.8537	0.8319
1.746	0.8860	0.9081	0.9012	0.8845
1.940	0.9158	0.9511	0.9433	0.9300
2.134	0.9417	0.9733	0.9730	0.9516
2.425	0.9559	0.9747	0.9816	0.9535
2.910	0.9534	0.9728	0.9770	0.9571
3.880	0.9598	0.9729	0.9716	0.9569

* [Jović and Driver (1994)]

Δ [Le, Moin and Kim (1997)]

♣ Fluent, version 6.3

inlet

$$\bar{V}_{in} = \frac{1}{\Delta y_{in}} \int_{y_{in}} v_x(y)\, dy + \frac{1}{\Delta y_{in}} \int_{y_{in}} v_y(y)\, dy, \tag{51}$$

and the outler surfaces

$$\bar{V}_{out} = \frac{1}{\Delta y_{out}} \int_{y_{out}} v_x(y)\, dy + \frac{1}{\Delta y_{out}} \int_{y_{out}} v_y(y)\, dy. \tag{52}$$

Ideally, the scaled difference η

$$\eta = \frac{\bar{V}_{in} - \bar{V}_{out}}{\bar{V}_{in}} \cdot 100\%. \tag{53}$$

284 between both average velocities should be zero to maintain the mass continuity. In
285 the laminar flow case, depicted in Figure 8.4: $\eta = 0.56\%$, in the turbulent flow
286 case, depicted in Figure 8.5: $\eta = 1.50\%$, and in the turbulent flow case, depicted
287 in Figure 8.9: $\eta = 1.36\%$, respectively.

Figure 8.11: he normalized velocity v_x at $x/H = 6$. Solid line – LRBFCM, dashed line – FLUENT, Δ - DNS and * - JD.

Table 3: Normalized velocity v_x at $x/H = 6$.

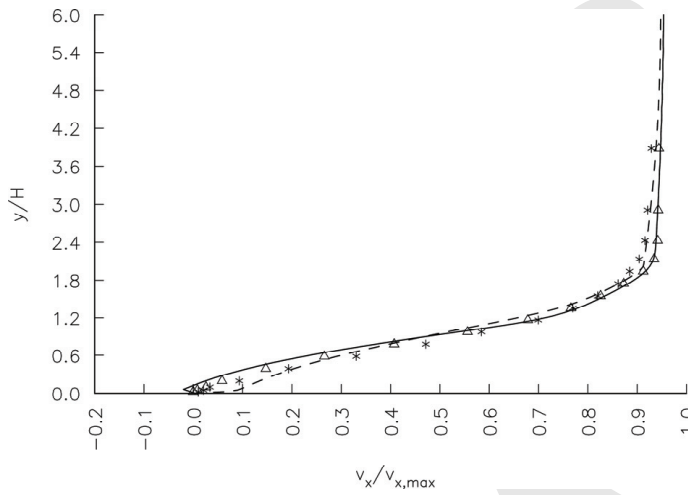|	experiment*	present method	DNS$^\Delta$	FVM$^\clubsuit$
0.025	0.0104	-0.0058	-0.0002	0.0668
0.049	0.0207	-0.0151	0.0083	0.0891
0.097	0.0337	-0.0083	0.0257	0.1052
0.194	0.0933	0.0246	0.0583	0.1347
0.388	0.1930	0.1097	0.1471	0.2037
0.582	0.3303	0.2248	0.2657	0.2915
0.776	0.4715	0.3700	0.4073	0.3970
0.970	0.5842	0.5384	0.5560	0.5154
1.164	0.6995	0.6931	0.6783	0.6362
1.358	0.7694	0.7788	0.7656	0.7395
1.552	0.8199	0.8346	0.8258	0.8106
1.746	0.8614	0.8814	0.8727	0.8622
1.940	0.8847	0.9164	0.9122	0.9025
2.134	0.9041	0.9329	0.9343	0.9148
2.425	0.9158	0.9383	0.9416	0.9195
2.910	0.9210	0.9415	0.9426	0.9268

Figure 8.12: The normalized velocity v_x at $x/H = 10$. Solid line – LRBFCM, dashed line – FLUENT, Δ - DNS and * - JD.

Table 4: Normalized velocity v_x at $x/H = 10$.

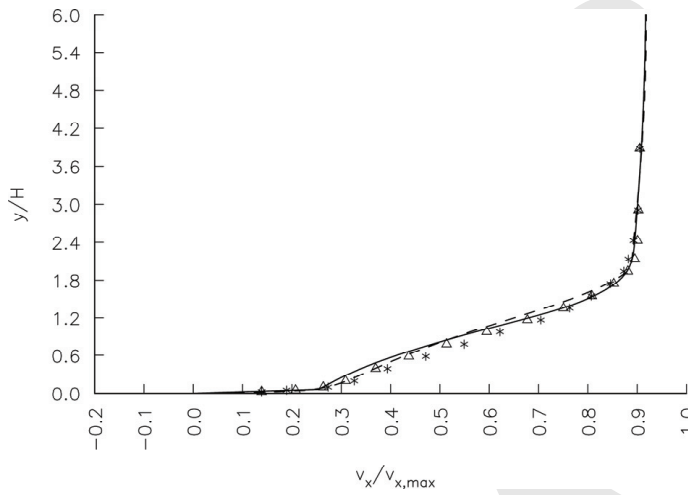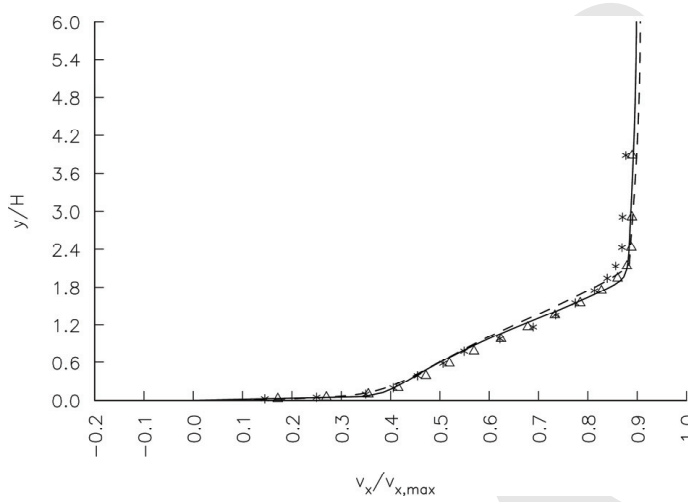|	experiment*	present method	DNS$^\Delta$	FVM$^\clubsuit$
0.025	0.1386	0.1035	0.1386	0.1737
0.049	0.1891	0.2028	0.2073	0.2285
0.097	0.2733	0.2625	0.2636	0.2706
0.194	0.3264	0.2864	0.3086	0.3102
0.388	0.3938	0.3400	0.3697	0.3677
0.582	0.4715	0.4064	0.4370	0.4262
0.776	0.5492	0.4850	0.5135	0.4911
0.970	0.6218	0.5728	05949	0.5620
1.164	0.7047	0.6642	0.6774	0.6371
1.358	0.7629	0.7483	0.7505	0.7124
1.552	0.8070	0.8119	0.8079	0.7822
1.746	0.8458	0.8546	0.8524	0.8398
1.940	0.8730	0.8792	0.8811	0.8797
2.134	0.8821	0.8898	0.8951	0.8893
2.425	0.8925	0.8952	0.9006	0.8928
2.910	0.9015	0.9000	0.9024	0.8989

Figure 8.13: The normalized velocity v_x at $x/H = 15$. Solid line – LRBFCM, dashed line – FLUENT, Δ - DNS and * - JD.

Table 5: The normalized velocity v_x at $x/H = 15$.

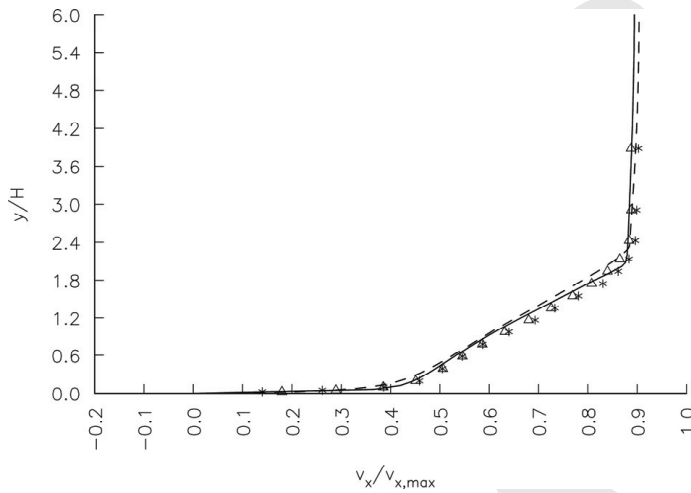|	experiment*	present method	DNS$^\Delta$	FVM$^\clubsuit$
0.025	0.1451	0.1416	0.1714	0.2011
0.049	0.2500	0.2775	0.2698	0.2721
0.097	0.3497	0.3687	0.3549	0.3361
0.194	0.4054	0.4062	0.4154	0.3895
0.388	0.4547	0.4513	0.4717	0.4473
0.582	0.5065	0.4959	0.5192	0.4944
0.776	0.5492	0.5449	0.5692	0.5415
0.970	0.6218	0.5985	0.6239	0.5906
1.164	0.6891	0.6559	0.6782	0.6420
1.358	0.7344	0.7154	0.7332	0.6951
1.552	0.7746	0.7745	0.7845	0.7485
1.746	0.8135	0.8299	0.8275	0.8000
1.940	0.8394	0.8703	0.8602	0.8467
2.134	0.8562	0.8800	0.8792	0.8815
2.425	0.8692	0.8837	0.8882	0.8862
2.910	0.8705	0.8867	0.8894	0.8908

Figure 8.14: The normalized velocity v_x at $x/H = 19$. Solid line – LRBFCM, dashed line – FLUENT, Δ - DNS and * - JD.

Table 6: The normalized velocity v_x at $x/H = 19$.

	experiment*	present method	DNS$^\Delta$	FVM$^\clubsuit$
0.025	0.1399	0.1495	0.1798	0.2068
0.049	0.2616	0.2931	0.2892	0.2823
0.097	0.3860	0.3975	0.3852	0.3551
0.194	0.4585	0.4458	0.4509	0.4174
0.388	0.5052	0.4910	0.5061	0.4785
0.582	0.5453	0.5296	0.5457	0.5225
0.776	0.5868	0.5693	0.5859	0.5634
0.970	0.6399	0.6115	0.6316	0.6045
1.164	0.6930	0.6562	0.6801	0.6466
1.358	0.7332	0.7031	0.7256	0.6898
1.552	0.7811	0.7513	0.7693	0.7337
1.746	0.8303	0.8000	0.8078	0.7775
1.940	0.8614	0.8498	0.8397	0.8196
2.134	0.8834	0.8778	0.8646	0.8575
2.425	0.8964	0.8814	0.8836	0.8853
2.910	0.8990	0.8840	0.8879	0.8894

Table 7: Reattachment length.

	reattachment length - x/H
experiment*	6.00±0.15
present method	6.28
DNS$^\Delta$	6.28
FVM♣	5.50

9 Conclusions

This paper probably for the first time represents the solution of the incompressible turbulent flow by a meshless method. Various turbulent models and numerical methods were used in the past to solve such kind of problems. In the present method, we used the low-Re k-ε model with the closure coefficients proposed by Jones and Launder (1971). Other low-Re turbulence models can be used in the present method [Wilcox (1993)], but the user should be careful about the boundary conditions for k and ε of each model. The numerical solution is based on the local collocation with the radial basis functions for spatial disretization and first order (backward Euler) explicit method for time discretization. Due to its locality and explicit time stepping, the method is very appropriate for parallelization. The partial differential equations are solved in their strong formulation, hence no integration are needed. The transition from two-dimensional to three-dimensional cases is quite straightforward. Three examples were focused to test the accuracy and applicability of the proposed method. In the first example, the laminar two-dimensional channel flow was simulated, where we show the capability of the fractional step method to solve the incompressible flows. The sparse solver was used to solve the pressure Poison's equation. The results were compared with the analytical solution and experiment. Turbulent flow in a two-dimensional channel and turbulent flow over a backward-facing step, were chosen in the next two examples, based on availability of the experimental and numerical tests. In the future, various casting problems [Vertnik and Šarler (2009)] will be simulated, where the heat and species transfer with solidification is involved in addition to the turbulent flow. With this, the new LRBFCM will most probably achieve reasonable maturity.

References

Atluri, S.N.; Shen, S. (2002): *The Meshless Method*, Tech Science Press, Encino.

Atluri, S.N. (2004): *The Meshless Method (MLPG) for Domain and BIE Discretization*, Tech Science Press, Forsyth.

Buhmann, M.D. (2000): *Radial Basis Functions*, Cambridge University Press, Cambridge.

Chen, C. S.; Ganesh, M.; Golberg, M. A.; Cheng, A. H. D. (2002): Multilevel compact radial basis functions based computational scheme for some elliptic problems. *Computers and Mathemathics with Applications*, vol. 43, pp. 359-378.

Chorin, A. J. (1967): A numerical method for solving incompressible viscous flow problems. *Journal of Computational Physics*, vol. 2, pp. 12-26.

Divo, E.; Kassab, A. J. (2007): An efficient localized RBF meshless method for fluid flow and conjugate heat transfer. *ASME Journal of Heat Transfer*, vol. 129, pp. 124-136.

Franke, J. (1982): Scattered data interpolation: tests of some methods. *Mathematics of Computation*, vol. 48, pp. 181-200.

Gu, Y.T.; Liu, G.R. (2005): Meshless technique for convection dominated problems. *Computational Mechanics*, vol. 38, pp. 171-182.

Haq, S.; ul-Islam, S.; Arshed, A. (2008): A numerical meshfree technique for the solution of the MEW equation, *CMES: Computer Modeling in Engineering & Sciences*, vol. 38, pp. 1-24.

Jones, W.P.; Launder, B.E. (1971): The prediction of laminarization with a two-equation model of turbulence. *International Journal of Heat and Mass Transfer*, vol. 15, pp. 301–314.

Jović, S.; Driver, D.M. (1994): Bacward-Facing Step Measurements at Low Reynolds Number, $Re_H = 5000$. *NASA Technical Memorandum 108807*.

Kansa, E. J. (1990b): Multiquadrics – a scattered data approximation scheme with application to computational fluid dynamics, part II. *Computers and Mathematics with Applications*, vol. 19, pp. 147-161.

Kansa, E. J. (1990a): Multiquadrics – a scattered data approximation scheme with application to computational fluid dynamics, part I. *Computers and Mathematics with Applications*, vol. 19, pp. 127-145.

Kosec, G.; Šarler, B.: (2008a): Solution of thermo-fluid problems by collocation with local pressure correction, *International Journal of Numerical Methods in Heat and Fluid Flow*, vol. 18. pp. 868-882.

Kosec, G.; Šarler, B. (2008b): Local radial basis function collocation method

for Darcy flow, *CMES: Computer Modeling in Engineering & Sciences*, vol.25, pp.197-207.

Kovačević, I.; Poredo?, A.; Šarler, B. (2003). Solving the Stefan problem with the radial basis function collocation method. *Numer. heat transf., B Fundam.*, vol. 44, pp. 1-24.

Kovačević, I.; Šarler, B. (2005): Solution of a phase-field model for dissolution of primary particles in binary aluminum alloys by an r-adaptive mesh-free method. *Materials Science and Engineering A*, vol. 413–414, pp. 423–428.

Laufer, J. (1948): Investigation of turbulent flow in a two-dimensional channel. *PHD Thesis*, California Institute of Technology, Pasadena, California.

Le, H.; Moin, P.; Kim, J. (1997): Direct numerical simulation of turbulent flow over a backward-facing step. *Journal of Fluid Mechanics*, vol. 330, pp. 349–374.

Le, P.; Mai-Duy, N; Tran-Cong, T.; Baker, G. (2008): A meshless modeling of dynamic strain localization in quasi-brittle materials using radial basic function networks, *CMES: Computer Modeling in Engineering & Sciences*, vol. 25, pp. 43-66.

Lee, C.K.; Liu, X.; Fan, S.C. (2003): Local multiquadric approximation for solving boundary value problems. *Computational Mechanics*, vol. 30, pp. 396–409.

Libre, N.A.; Emdadi, A.; Kansa, E.J.; Rahimian, M.; Shekarchi, M. (2008): A stabilised RBF collocation scheme for Neumann type boundary conditions. *CMES: Computer Modeling in Engineering & Sciences*, vol. 24, pp. 61–80.

Lin, H., Atluri, S.N.. (2000) Meshless local Petrov-Galerkin (MLPG) method for convection-diffusion *CMES: Computer Modeling in Engineering & Sciences*, vol.1. 45-60.

Lin, H, Atluri, S.N. (2001) The Meshless Local Petrov-Galerkin (MLPG) method for solving incompressible Navier-Stokes equations, *CMES: Computer Modeling in Engineering & Sciences*, vol. 2, pp. 117-142.

Liu, G.R. (2003): *Mesh Free Methods*, CRC Press, Boca Raton.

Liu, G.R.; Gu, Y.T. (2005): *An Introduction to Meshfree Methods and Their Programming*, Springer, Dordrecht.

Mai-Cao, L.; Tran-Cong, T. (2005): A meshless IRBFN-based method for transient problems, *CMES: Computer Modeling in Engineering & Sciences*, vol. 7, pp. 149-171.

Mai-Cao, L.; Tran-Cong, T. (2008): A meshless approach to capturing moving interfaces in passive transport problems, *CMES: Computer Modeling in Engineering & Sciences*, vol. 31, pp. 157-188.

    CMES, vol.1189, no.1, pp.1-31, 2009

Mai-Duy, N.; Tran-Cong, T. (2003): Indirect RBFN method with thin plate splines for numerical solution of differential equations, *CMES: Computer Modeling in Engineering & Sciences*, vol. 4, pp. 85-102.

Mai-Duy, N.; Khennane, A.; Tran-Cong, T. (2007): Computation of laminated composite plates using integrated radial basis function networks, *CMC: Computers, Materials, & Continua*, vol. 5, pp. 63-78.

Mai-Duy, N.; Mai-Cao, L.; Tran-Cong, T. (2007): Computation of transient viscous flows using indirect radial basic function networks, *CMES: Computer Modeling in Engineering & Sciences*, vol. 18, pp. 59-77.

Perko, J.; Šarler, B. (2007): Weigh function shape parameter optimization in meshless methods for non-uniform grids. *CMES*, vol. 19, pp. 55-68.

Shu, C.; Ding, H.; Yeo, K. S. (2005): Computation of incompressible Navier-Stokes equations by local RBF-based differential quadrature method. *CMES*, vol. 7, pp. 195-205.

Šarler, B. (2005): A radial basis function collocation approach in computational fluid dynamics. *CMES: Computer Modelling in Engineering & Sciences*, vol. 7, pp. 185-193.

Šarler, B. (2007): From global to local radial basis function collocation method for transport phenomena, *Advances in Meshfree Techniques*, Springer, Berlin, pp. 257-282.

Šarler, B.; Perko, J.; Chen, C. S.; Kuhn, G. (2001): A meshless approach to natural convection, *International Conference on Computational Engineering and Sciences, CD proceedings.*

Šarler, B.; Vertnik, R. (2006): Meshfree explicit local radial basis function collocation method for diffusion problems. *Computers and Mathematics with Applications*, vol. 51, pp. 1269-1282.

Vertnik, R.; Šarler, B. (2006): Meshless local radial basis function collocation method for convective-diffusive solid-liquid phase change problems. *International Journal of Numerical Methods for Heat and Fluid Flow*, vol. 16, pp. 617-640.

Vertnik, R.; Zalonik, M.; Šarler, B. (2006): Solution of transient direct-chill aluminium billet casting problem with simultaneous material and Interphase moving boundaries by a meshless method. *Engineering Analysis with Boundary Elements*, vol. 30, pp. 847-855.

Vertnik, R.; Šarler, B.; Bulinski, Z.; Manojlović, G. (2007): Solution of transient temperature field in continuous casting of steel by a meshless method, *Second International Conference of Simulation and Modelling of Metallurgical Processes in Steelmaking*, Graz, Austria, September 2007, ASMET.

426 **Vertnik, R.; Šarler, B.;** (2009): Solution of continuous casting of steel by a mesh-
427 less method, *Cast Metals Research*, 2009, in print.

428 **Wilcox, D.C.** (1993): *Turbulence modeling for CFD*, DCW Industries, California.

429 **Yoder, D. A.; Georgiadis, N. J.** (1999): Implementation and validation of the
430 Chien k-ε turbulence model in the Wind Navier-Stokes code, *NASA Technical*
431 *Memorandum 209080.*

432